

Maximized Effective Energy Output of Contact-Separation-Triggered Triboelectric Nanogenerators as Limited by Air Breakdown

Yunlong Zi, Changsheng Wu, Wenbo Ding, and Zhong Lin Wang*

Recent progress in triboelectric nanogenerators (TENGs) has demonstrated their promising potential as a high-efficiency mechanical energy harvesting technology, and plenty of effort has been devoted to improving the power output by maximizing the triboelectric surface charge density. However, due to high-voltage air breakdown, most of the enhanced surface charge density brought by material/surface optimization or external ion injection is not retainable or usable for electricity generation during the operation of contact-separation-triggered TENGs. Here, the existence of the air breakdown effect in a contact-separation mode TENG with a low threshold surface charge density of $\approx 40\text{--}50 \mu\text{C m}^{-2}$ is first validated under the high impedance external load, and then followed by the theoretical study of the maximized effective energy output as limited by air breakdown for contact-separation-triggered TENGs. The effects of air pressure and gas composition are also studied and propose promising solutions for reducing the air breakdown effect. This research provides a crucial fundamental study for TENG technology and its further development and applications.

1. Introduction

To sustainably power trillions of small electronics distributed in every corner of the world, nanogenerators^[1] have been invented to harvest energy in ambient environment. Among them, triboelectric nanogenerators (TENGs)^[2–4] based on coupling of triboelectrification and electrostatic induction effects have been rapidly developed since 2012. The detailed working principle of TENG is illustrated in Figure S1 and Note S1 (Supporting Information). To quantitatively evaluate the output performance, figure-of-merits (FOM) of TENG have been developed based on cycles of maximized energy output, in which the maximized energy output per cycle E_m has quadratic dependence on triboelectric surface charge density.^[5] Compared with sliding-triggered

TENGs, TENGs as triggered by contact-separation process (contact-separation-triggered TENGs) have shown advantages of high structural FOM,^[5] facile packaging, and minimal abrasion. However, in contact-separation-triggered TENGs, air breakdown effect has been demonstrated to be the culprit of electrostatic discharge which leads to limited charge density retainable on triboelectric surfaces.^[6,7] As numerous efforts have been made to push the surface charge density to approach its limit,^[8–18] such breakdown effect has become the major limitation on the output performance.

As limited by the air breakdown effect, the maximum surface charge density for contact-separation (CS) mode TENG is around $240 \mu\text{C m}^{-2}$ in the short-circuit condition.^[6,8] However, this limit of the charge density cannot reflect the realistic limitation of the output energy because there is no energy output in the short-circuit condition.

During practical operations, the air breakdown may happen with a charge density below $240 \mu\text{C m}^{-2}$, since under the external load with a higher impedance, it is possible to produce much higher potential difference between triboelectric surfaces than that in the short-circuit condition.^[19] The maximized effective energy output as limited by air breakdown, which is the most crucial limitation for output performance of TENGs, is still required to be revealed by studies of air breakdown in TENGs through voltage–charge transfer ($V\text{--}Q$) plots.^[5] It is also demanded to study the air breakdown effect in other contact-separation-triggered TENGs, such as contact freestanding-triboelectric-layer (CFT) mode and single-electrode-contact (SEC) mode TENGs.

Here, we first confirm the existence of air breakdown for CS mode TENG with a low threshold surface charge density of $\approx 40\text{--}50 \mu\text{C m}^{-2}$, through both theoretical calculations and experiments. The breakdown areas of contact-separation-triggered TENGs (CS, CFT, and SEC modes) are illustrated in their $V\text{--}Q$ plots, as calculated by Paschen's law and theories of TENGs.^[20–23] And then the maximized effective energy outputs per cycle of TENGs as limited by air breakdown are calculated and plotted versus the charge density. To improve the output performance by reducing the effects from air breakdown, TENGs operated in air with different pressures or gas environments are explored. This research provides guidance on both design and operation for TENGs, which will make a solid step toward commercialization and applications of TENG technology.

Dr. Y. Zi, C. Wu, Dr. W. Ding, Prof. Z. L. Wang
School of Materials Science and Engineering
Georgia Institute of Technology
Atlanta, GA 30332-0245, USA
E-mail: zhong.wang@mse.gatech.edu
Prof. Z. L. Wang
Beijing Institute of Nanoenergy and Nanosystems
Chinese Academy of Sciences
National Center for Nanoscience and Technology (NCNST)
Beijing 100083, P. R. China

DOI: 10.1002/adfm.201700049

2. Existence of the Air Breakdown Effect

Electrical breakdown is a common phenomenon for electrostatic discharge in various devices.^[24–27] In particular, air breakdown is likely to happen in contact-separation-triggered TENGs between the two triboelectric surfaces with opposite static charges, due to the high voltage created in the vertical separation process.^[19,28,29] As compared with other discharging effects including drift,^[10] diffusion,^[30] and charge recombination^[31] which all take relative long time for decreasing the charge density, the air breakdown effect usually results in immediate discharging of the surface charge, and hence we consider it as the key limitation of the output performance of TENG. The threshold voltage for air breakdown between two parallel plates is described by Paschen's law^[32]

$$V_b = \frac{Bpd}{\ln(Apd) - \ln\left[\ln\left(1 + \frac{1}{\gamma_{se}}\right)\right]} \quad (1)$$

Here V_b is the threshold breakdown voltage, p is the pressure, d is the gap distance between the boards, constant γ_{se} is the secondary electron emission coefficient, constant A is the saturation ionization in the gas, and constant B is related to the excitation and ionization energies. The threshold breakdown voltage V_b as calculated by Paschen's law for 1 atm air is plotted in **Figure 1a**, in which that for distance d of 0.01 m is 36 142 V.

To prove the existence of air breakdown in CS mode TENG with low surface charge density, we consider one typical device as shown in inset of **Figure 1a**, with both length l and width w of 0.1 m, displacement x (equivalent to d) of 0.01 m, dielectric thickness d_r of 0.1 mm, relative dielectric constant ϵ_r of 0.5, and charge density σ of 70 $\mu\text{C m}^{-2}$. The voltage V_1 between the triboelectric surfaces at $x = 0.01$ m in short-circuit condition is calculated to be only about ≈ 390 V, with edge effects considered^[33] (all the calculations are in 1 atm air atmosphere unless otherwise specified, also see the Experimental Section). This voltage is far lower than V_b , as denoted by dot E in **Figure 1a**. However, if TENG is operated under high-impedance-load condition, i.e., there is a nonzero voltage V between two electrodes depending on the charge transfer Q (here we use the minimum achievable charge reference state^[21]), V_1 might be higher at the same $x = 0.01$ m (as denoted by dots A–D, corresponding to $Q = 0$, 1.75×10^{-7} , 3.5×10^{-7} , and 5.25×10^{-7} C, respectively). Based on calculations (see methods in Note S2 and **Figure S2** in the Supporting Information), both $V_1(\text{A})$ and $V_1(\text{B})$ exceed V_b of 36 142 V. To cross-check our calculations, we also simulate the potential distributions of TENG in statuses A–D by finite element method using COMSOL Multiphysics software (**Figure 1b**), which verifies $V_1(\text{A})$ and $V_1(\text{B})$ are both higher than V_b (see methods in Note S3 in the Supporting Information). Therefore, to reveal all the circumstances with existence of air breakdown in this TENG, we calculate the V_1 and V_b with various given x and Q , and plot them as **Figure 1c,d** (see methods in Note S2 and **Figure S2** in the Supporting Information). The difference between the two voltages $V_b - V_1$ is also calculated, as plotted in **Figure 1e**, in which the negative value means $V_b < V_1$ and indicates a breakdown area (marked by “–”).

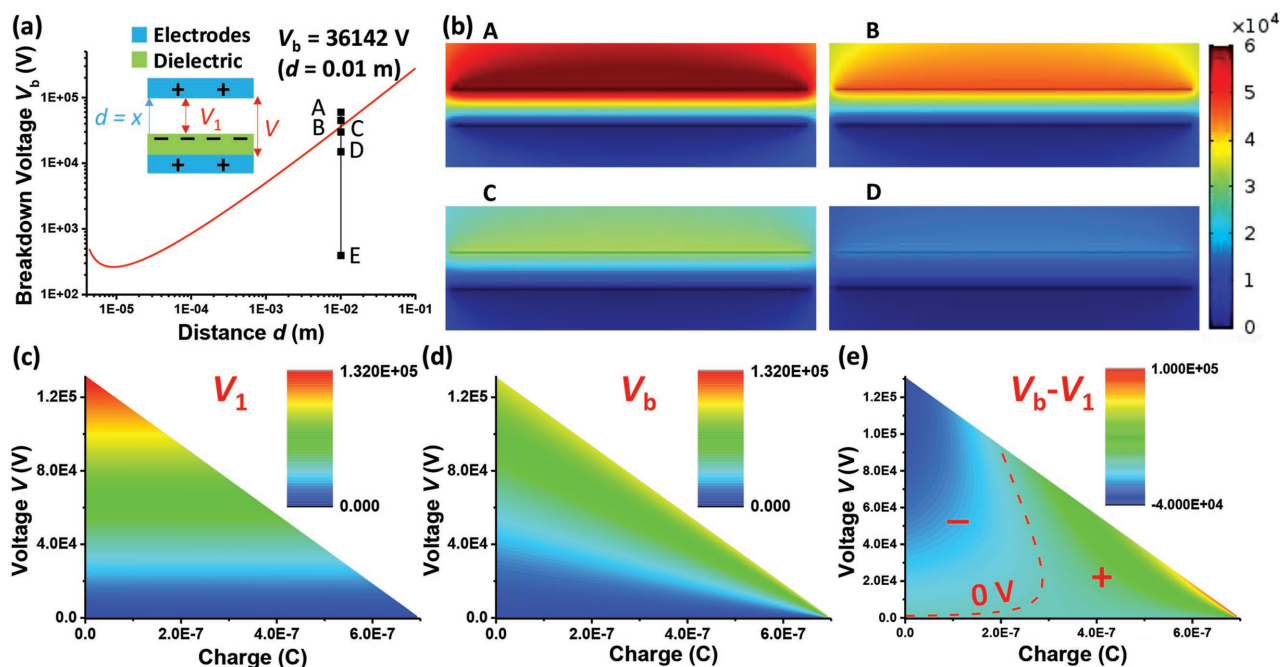


Figure 1. The existence of air breakdown effect in a CS mode TENG with a low charge density. a) The breakdown voltage as calculated by Paschen's law in 1 atm air, in which the points A–E show the voltage V_1 between triboelectric surfaces of the CS mode TENG under different charge transfers Q . The inset shows the schematic diagram of the TENG. b) The potential distribution of A–D as simulated by COMSOL Multiphysics software. c) The distribution of the voltage V_1 between triboelectric surfaces in V – Q plot. d) The distribution of the breakdown voltage V_b in V – Q plot. e) The distribution of $V_b - V_1$ in V – Q plot, with the contour line of 0 V displayed as the red dashed line. The positive (“+”) and negative (“–”) areas are divided by this contour line.

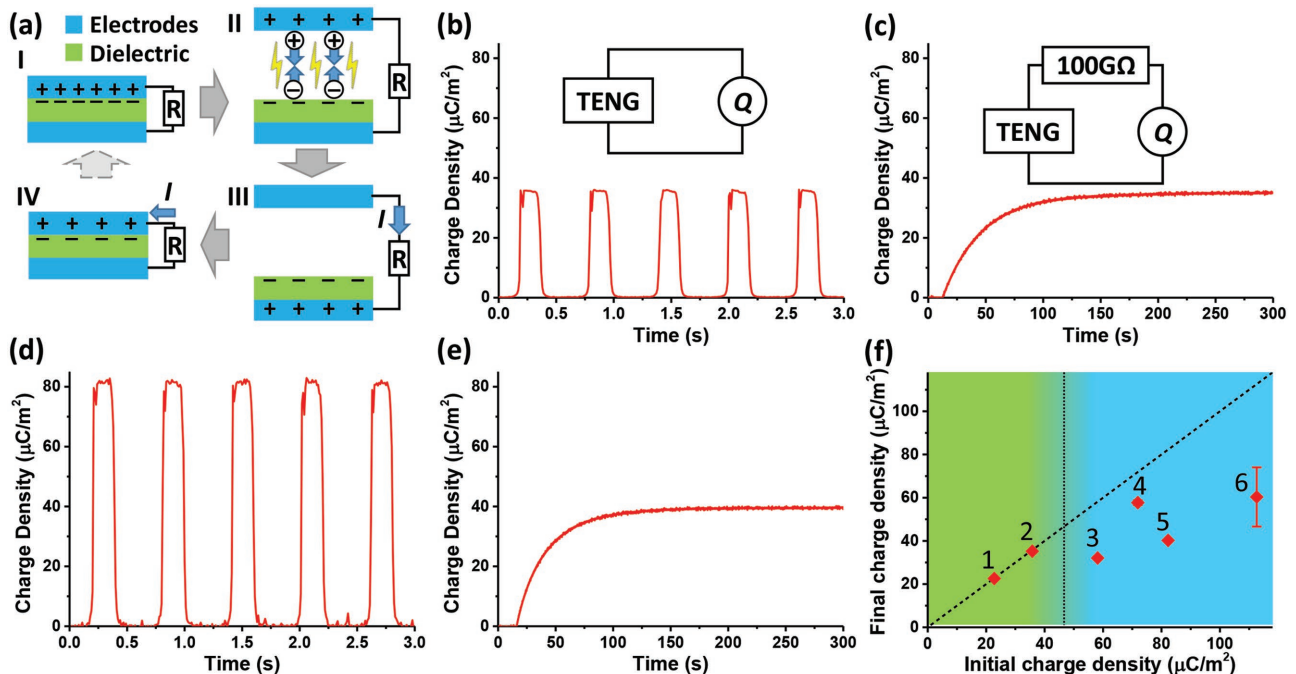


Figure 2. The experiment to demonstrate the existence of air breakdown with a low threshold surface charge density. a) The process of the air breakdown during CS mode TENG operation and the mechanism of the final charge density measurement. b,c) The initial and final charge density measurements with initial charge density of $\approx 35.8 \mu\text{C m}^{-2}$. The insets show the corresponding circuits. d,e) The initial and final charge density measurements with initial charge density of $\approx 82.3 \mu\text{C m}^{-2}$. f) The test results of final charge densities for six TENGs. The dashed inclined line indicates equal initial and final charge densities, and the dotted vertical line indicates σ_1 which separates σ_0 without breakdown (green) and with breakdown (blue).

We can notice that in this V - Q plot, the breakdown area is with low charge transfer Q and high voltage V between electrodes, which is easily achieved in the high-impedance-load condition. The contour with $V_b - V_1 = 0 \text{ V}$ is also plotted inside as the red dashed line, outlining the boundary of this breakdown area. These results indicate the existence of the air breakdown effect in the CS mode TENG with charge density of only $70 \mu\text{C m}^{-2}$.

To further verify the existence of air breakdown in CS mode TENG with low charge density, we designed an experiment to monitor charge transfers in the short circuit and the high-impedance-load conditions, respectively. The mechanism of the designed experiment is proposed in **Figure 2a**. Initially in **Figure 2a-I**, TENG is in contact status ($x = 0$), with the initial surface charge density σ_0 . In **Figure 2a-II**, when the TENG is operated from $x = 0$ to $x = x_{\text{max}}$ with a large external load resistance, due to the obstructed charge transfer brought by the large resistance, most of positive charges remain in the top electrode and hence air breakdown may happen due to the high voltage induced by these positive charges. In **Figure 2a-III**, after motion stops at $x = x_{\text{max}}$, the residual charges gradually transfer to the bottom electrode. And then as shown in **Figure 2a-IV**, when TENG is operated back to $x = 0$, the residual charge can be gradually transferred back to the top electrode. From III to IV, we can monitor the transfer amount of the residual charge and calculate the final charge density σ_1 . Here we consider the difference between σ_0 and σ_1 is mainly due to the breakdown effect, since the other effects induced discharging process^[10,30,31] usually take a long time (at least several hours) as stated above. Therefore, if $\sigma_0 > \sigma_1$ dramatically, the breakdown happens; if $\sigma_0 \approx \sigma_1$, there is no breakdown effect. The surface

charge density can be recovered back to status I by triboelectrification or ionized-air injection.^[6]

We measured six CS mode TENGs with different initial charge densities achieved by different materials and treatments (see the Experimental Section).^[6,9] For TENG #2 with σ_0 of $\approx 35.8 \mu\text{C m}^{-2}$ (Figure 2b, measured in the short-circuit condition, with the circuit shown in inset), σ_1 was measured as $\approx 35.2 \mu\text{C m}^{-2}$ (Figure 2c, with $100 \text{ G}\Omega$ resistance as the large load resistance, and the circuit is shown in inset), which is almost the same as σ_0 . However, for TENG #5 with σ_0 of $\approx 82.3 \mu\text{C m}^{-2}$ (Figure 2d), σ_1 was measured as only $\approx 40.2 \mu\text{C m}^{-2}$ (Figure 2e) which is much lower than σ_0 . The measurement results for all the six TENGs are plotted in **Figure 2f**. We can notice that for TENGs #1 and #2 with relative low σ_0 , $\sigma_0 \approx \sigma_1$; and for TENGs #3–6 with relative high σ_0 , $\sigma_0 > \sigma_1$. The decreases in the charge densities for TENG #3–6 were observed immediately after the very first half-cycle of TENG operation with the load resistance of $100 \text{ G}\Omega$. These results indicate the existence of air breakdown for TENG operated in high-impedance-load condition with the charge density much lower than the threshold for the short-circuit condition ($240 \mu\text{C m}^{-2}$), and the corresponding threshold surface charge density σ_1 is around only 40 – $50 \mu\text{C m}^{-2}$.

3. Breakdown Areas and Maximized Effective Energy Output

To systematically study the air breakdown effects in CS, CFT, and SEC mode TENGs, their breakdown areas are determined by comparing V_1 and V_b as described above. Their

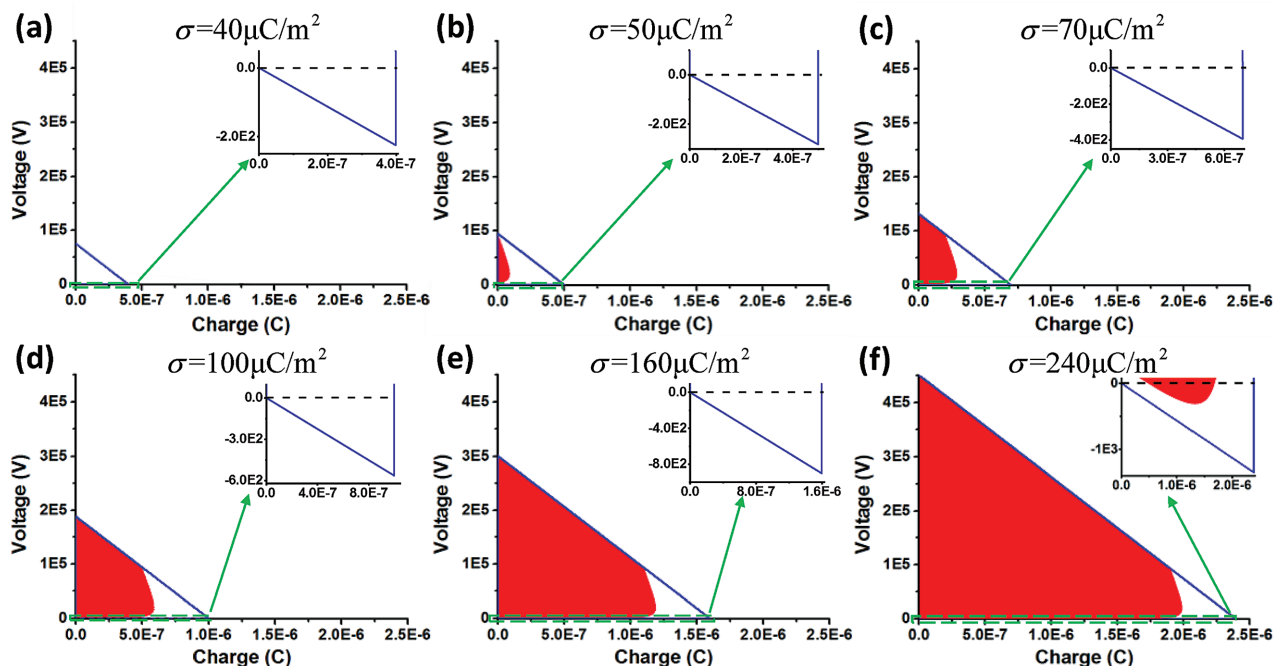


Figure 3. The breakdown areas (in red) of CS-mode TENG with various charge densities. The insets show the areas with $V \leq 0$.

V - Q plots with different surface charge densities are calculated and plotted in **Figures 3–5**, in which the breakdown areas are highlighted in red. For CFT mode, air breakdown may happen between both pairs of triboelectric surfaces, and hence there are usually two breakdown areas displayed

(Figure 4). The parameters selected for these TENGs are listed in **Table 1**.

As shown in Figure 3a, there is no air breakdown happens in CS mode TENG with $40 \mu\text{C m}^{-2}$. TENG with $50 \mu\text{C m}^{-2}$ begins to have a small breakdown area as shown in Figure 3b.

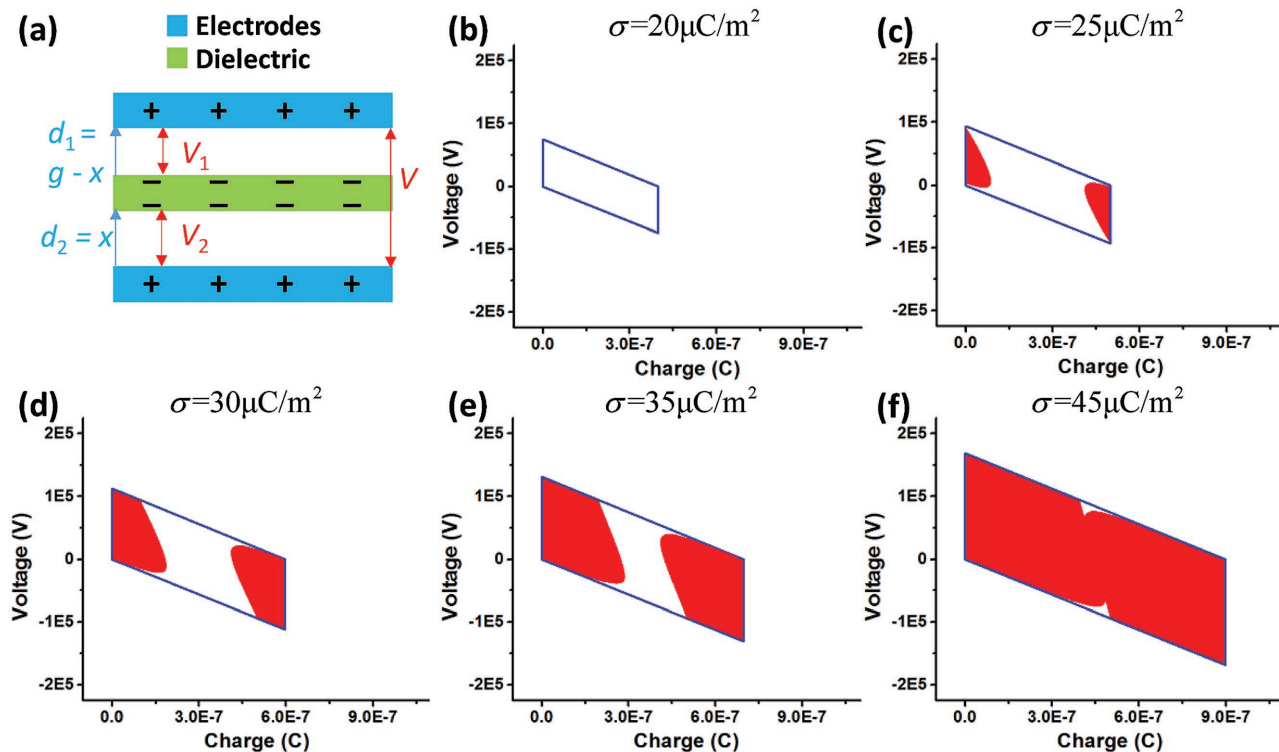


Figure 4. a) The schematic diagram and b–f) the breakdown areas (in red) of CFT mode TENG with various charge densities.

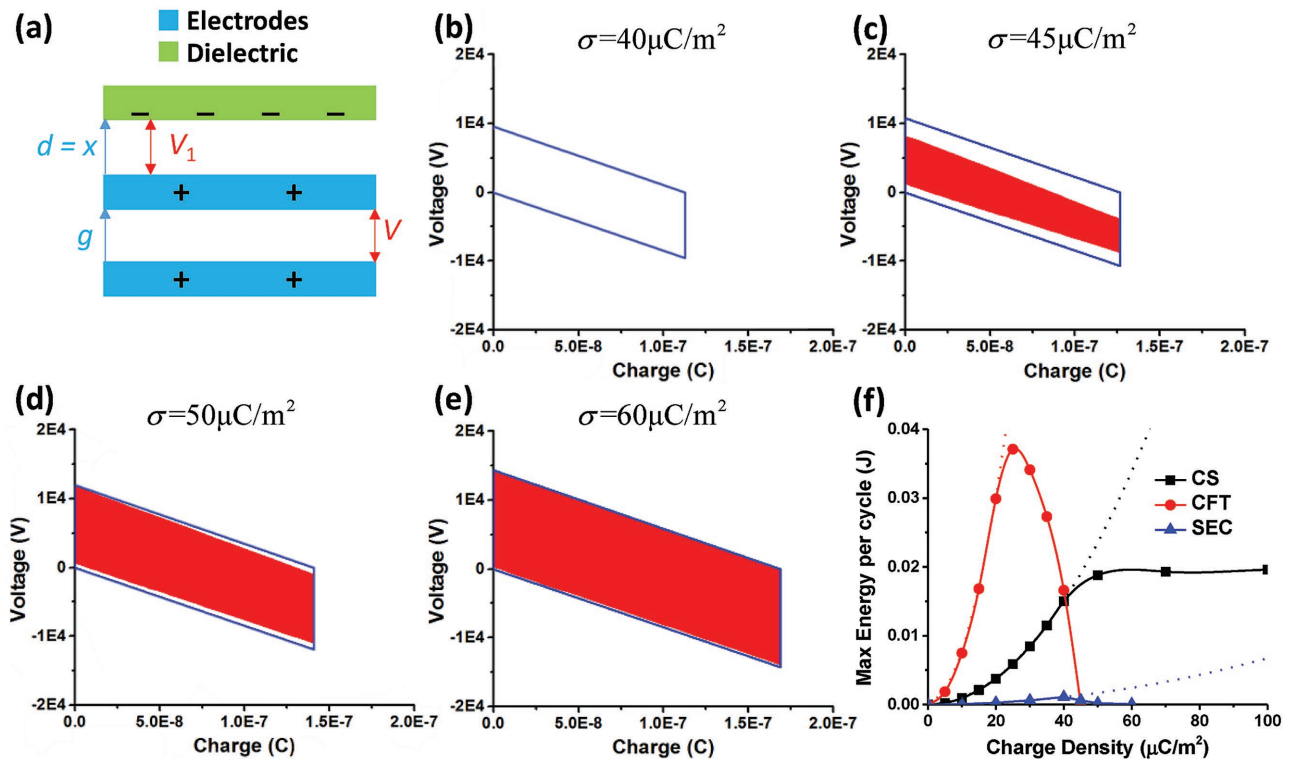


Figure 5. a) The schematic diagram and b–e) the breakdown areas (in red) of SEC mode TENG with various charge densities. Panel (f) shows the maximized effective energy output per cycle for three modes TENGs.

This result indicates the threshold surface charge density σ_t is about $40\text{--}50\ \mu\text{C m}^{-2}$, which is consistent with the experimental result in Figure 2. Without consideration of the air breakdown effect, the maximized energy output per cycle E_m , which is the area enclosed by blue lines in Figure 3, is proportional to the square of σ .^[5] The breakdown area also increases with σ , as shown in Figure 3c–f. The maximized effective energy output per cycle E_{em} can be defined as the area of E_m subtracting the breakdown area in each figure. As summarized later in Figure 5f, E_{em} saturates at around $0.02\ \text{J}$ even though σ continues to increase. We also zoomed in the negative-voltage part of each $V\text{--}Q$ plot in the inset of each one. We notice that when σ approaches $\approx 240\ \mu\text{C m}^{-2}$, the red breakdown area begins to overlap with Q -axis, i.e., the route of the short-circuit condition, which is consistent with the short-circuit maximum charge density of $\approx 240\ \mu\text{C m}^{-2}$ as reported previously.^[6]

Table 1. Parameters of TENGs for calculations.

TENG mode	CS	CFT	SEC
Dielectric layer	Thickness $d_i = 0.1\ \text{mm}$, dielectric constant $\epsilon_r = 2$, so effective thickness $d_0 = d_i/\epsilon_r = 0.05\ \text{mm}$ ^[20]		
Area	Length $l \times$ width w : $0.1\ \text{m} \times 0.1\ \text{m}$		
Gap g between electrodes [m]	Not Applicable	0.03	0.01
Charge density [$\mu\text{C m}^{-2}$]	0–250	0–180	0–210
Displacement x [m]	0–0.03		

Similarly, the breakdown areas for CFT and SEC mode TENGs with different charge densities are also calculated, as shown in Figures 4 and 5. The schematic diagrams for CFT and SEC mode TENGs are shown in Figures 4a and 5a, respectively. The two breakdown areas in CFT mode TENGs are calculated separately and plotted together in each plot in Figure 4. Unlike CS mode TENG, when the charge density σ is larger than the threshold air breakdown charge density σ_t , E_{em} of CFT mode and SEC mode TENGs quickly decrease to approach 0 with the increase of σ . E_{em} versus σ for all the TENGs are plotted as dots and solid lines in Figure 5f, while E_m without considering air breakdown are also plotted as the dashed lines for comparison. We notice that even though CFT mode TENG always has the largest E_m due to the highest structural FOM,^[5] its output performance is actually limited by the low threshold charge density σ_t of $20\text{--}25\ \mu\text{C m}^{-2}$. On the contrary, σ_t of CS and SEC mode TENGs are both about $40\text{--}50\ \mu\text{C m}^{-2}$. Besides, when $\sigma > \sigma_t$, E_{em} of CFT mode TENG approaches 0 at $\approx 45\ \mu\text{C m}^{-2}$. In another word, air breakdown effect is more prone to happen in CFT mode TENG compared to other modes TENG, resulting in suppressed output performance of CFT mode TENG. Considering low structural FOM of SEC mode TENG,^[5] CS mode TENG usually has the largest effective energy output in all the three modes of TENGs, with broad applications demonstrated.^[34–38]

To further estimate the practical energy output available in the nonbreakdown areas

for applications, we also calculated the largest energy storage per cycle while charging a battery through the designed charging cycles.^[39] To achieve the largest energy storage, the displacement x of each TENG is limited in a certain range to avoid the breakdown areas. The largest energy storage as well as the maximized energy output might be achieved through automatic switches built in TENG.^[39–41] We notice that the trend of the largest energy storage per cycle is similar to that of E_{em} with increase of charge density σ . The detailed results and methods are shown in Figure S3 and Note S4 (Supporting Information).

4. Maximized Effective Energy Output as Affected by Ambient Environment

Since air breakdown effect highly depends on ambient environment, we explored the air breakdown limits of TENG in air with different pressures and in gas atmosphere. Curves of Paschen's law for air under 1, 2, 5 atm pressures, and SF₆ gas under 1 atm pressure are plotted in Figure 6a. We notice that with the increase of air pressure, the Paschen's curve shifts toward left and the threshold breakdown voltages V_b increases for most of gap distance d , which is due to the lower mean-free-path and the smaller kinetic energy accumulated in electrons. On the contrary, for air under lower pressure, the whole curve moves right, which makes air breakdown easier with low vacuum level (usually 10⁻⁴–1 atm). However, if the pressure is even lower, since the density of the air molecules is extremely low, it becomes difficult for the air breakdown effect. For instance, in 10⁻⁶ atm air, the distance d needs to be as high as about 3 m to have the air breakdown effect (Figure S4,

Supporting Information), which means there is actually no air breakdown effect in such ultralow pressure environment for common TENGs with limited displacement. For SF₆ gas, V_b is always higher than that of air, since SF₆ with higher molecular weight is much more difficult to be ionized by electrons.^[42]

E_{em} versus σ under different environments for TENGs are also calculated as plotted in Figure 6b–d. As we notice, the trend of each E_{em} curve is similar for the same mode TENG, but TENGs operated in higher air pressures or SF₆ always have higher breakdown limits and higher E_{em} available. This result indicates a possible solution to improve TENG outputs in harsh environments, by fully packaging TENGs with air in high pressure or high-breakdown-limit gas environments. This type of fully packaged TENGs can be indirectly driven by acoustic waves or magnetic field.^[43–45]

5. Conclusions

In summary, we first demonstrate the existence of air breakdown in CS mode TENG with a low threshold surface charge density of ≈ 40 –50 $\mu\text{C m}^{-2}$, through both theoretical calculations and experiments. We calculate maximized effective energy outputs per cycle for CS, CFT, and SEC modes, which show suppressed energy output capability due to the air breakdown effect. In these three modes, air breakdown is more prone to happen in CFT mode TENG, which greatly limits its output performance. The breakdown areas for TENGs operated in air with different pressures and in SF₆ gas are also calculated and compared with that in 1 atm air, providing potential solutions to enhance the output performance of TENGs by reducing the breakdown effect. This research provides a crucial fundamental

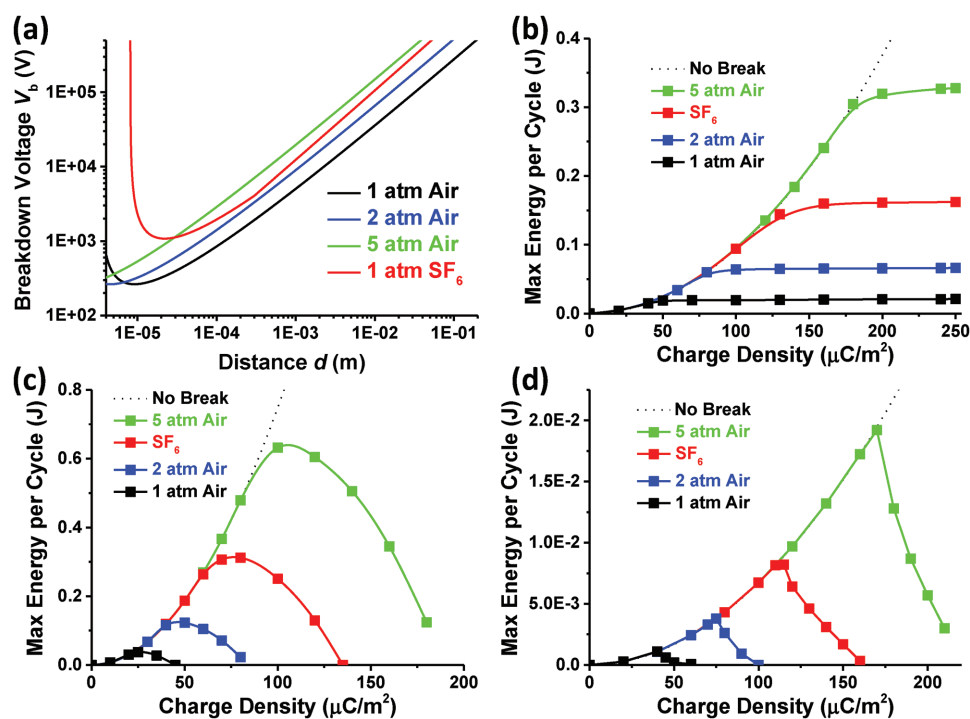


Figure 6. a) Plots of the Paschen's law and b–d) the maximized effective energy output per cycle for three modes TENG in different environments.

study for further development and applications of TENG technology.

6. Experimental Section

Calculation of the Voltage between Triboelectric Surfaces: The most crucial part is the capacitance between triboelectric surfaces, which is calculated by considering two-side edge effects of the nonideal parallel-plate capacitor. The equation is listed below^[33]

$$C = \epsilon_0 \epsilon_r \left\{ \frac{lw}{d} + \frac{l}{\pi} \left[1 + \ln \left(1 + 2\pi \frac{w}{d} + \ln \left(1 + 2\pi \frac{w}{d} \right) \right) \right] + \frac{w}{\pi} \left[1 + \ln \left(1 + 2\pi \frac{l}{d} + \ln \left(1 + 2\pi \frac{l}{d} \right) \right) \right] \right\} \quad (2)$$

With the calculated capacitance and considering the effective charge amount in the capacitor formed by the triboelectric surfaces, the voltage can be calculated to compare with V_b . The detailed equations to calculate the voltages between triboelectric surfaces and between electrodes are listed in Note S2 (Supporting Information). The calculation methods of $V_{OC,max}$, $Q_{SC,max}$, and V_{max} are as same as that in a previous paper.^[5]

Preparation, Treatments, and Measurement of CS-Mode TENGs: Six TENGs were all fabricated with the same area of 4.5 cm × 4.5 cm and maximum displacement of 1 cm. The different charge densities come from the different triboelectric materials and treatments.

For TENGs #1 and #2, the 100 nm Ti film was first deposited on cut glass slides by e-beam evaporation as one electrode, and then the silicon oxide (SiO₂) films were deposited by a plasma-enhanced chemical vapor deposition method as one triboelectric material. The counter triboelectric material as well as the other electrode is a copper (Cu) foil attached on an acrylic board. The SiO₂/Ti/glass slide of TENG #2 was immersed in 1% (in volume ratio) (3-aminopropyl)triethoxysilane solutions in ethanol for 12 h to improve the charge density.^[9]

For TENGs #3–#6, the 100 nm gold (Au) films were first deposited on Kapton substrates by using an e-beam evaporator as one triboelectric material and one electrode. Fluorinated ethylene propylene films were used as the other triboelectric material, with deposited Cu films on the back side as the other electrode. The Au/Kapton films of TENGs #4 and #5 were first cleaned with O₂ plasma for 2 min and then immersed in 5 × 10⁻³ M (#4) and 10 × 10⁻³ M (#5) 2-mercaptoethanol solutions in ethanol for 12 h, to enhance the surface charge density.^[9] For TENG #6, the ionized-air-injection method was performed by an air-ionization gun to greatly improve the charge density.^[6]

The motion of the TENGs were triggered by a linear motor, and the measurements of the transferred charges were conducted by a Keithley 6514 electrometer.

Supporting Information

Supporting Information is available from the Wiley Online Library or from the author.

Acknowledgements

Y.Z. and C.W. contributed equally to this work. This research was supported by the National Science Foundation (DMR-1505319), the KAUST, the Hightower Chair foundation, and the “Thousands Talents” program for pioneer researcher and his innovation team, China.

Conflict of Interest

The authors declare no conflict of interest.

Keywords

electrical breakdown, energy harvesting, nanogenerators, output performance

Received: January 4, 2017

Revised: March 19, 2017

Published online:

- [1] Z. L. Wang, J. Song, *Science* **2006**, 312, 242.
- [2] F.-R. Fan, Z.-Q. Tian, Z. L. Wang, *Nano Energy* **2012**, 1, 328.
- [3] Z. L. Wang, *ACS Nano* **2013**, 7, 9533.
- [4] Z. L. Wang, *Faraday Discuss.* **2014**, 176, 447.
- [5] Y. Zi, S. Niu, J. Wang, Z. Wen, W. Tang, Z. L. Wang, *Nat. Commun.* **2015**, 6, 8376.
- [6] S. Wang, Y. Xie, S. Niu, L. Lin, C. Liu, Y. S. Zhou, Z. L. Wang, *Adv. Mater.* **2014**, 26, 6720.
- [7] Z. Su, M. Han, X. Cheng, H. Chen, X. Chen, H. Zhang, *Adv. Funct. Mater.* **2016**, 26, 5524.
- [8] J. Wang, S. Li, F. Yi, Y. Zi, J. Lin, X. Wang, Y. Xu, Z. L. Wang, *Nat. Commun.* **2016**, 7, 12744.
- [9] S. Wang, Y. Zi, Y. S. Zhou, S. Li, F. Fan, L. Lin, Z. L. Wang, *J. Mater. Chem. A* **2016**, 4, 3728.
- [10] N. Cui, L. Gu, Y. Lei, J. Liu, Y. Qin, X. Ma, Y. Hao, Z. L. Wang, *ACS Nano* **2016**, 10, 6131.
- [11] J. Wang, Z. Wen, Y. Zi, P. Zhou, J. Lin, H. Guo, Y. Xu, Z. L. Wang, *Adv. Funct. Mater.* **2016**, 26, 1070.
- [12] J. Chun, J. W. Kim, W.-S. Jung, C.-Y. Kang, S.-W. Kim, Z. L. Wang, J. M. Baik, *Energy Environ. Sci.* **2015**, 8, 3006.
- [13] C. K. Jeong, K. M. Baek, S. Niu, T. W. Nam, Y. H. Hur, D. Y. Park, G.-T. Hwang, M. Byun, Z. L. Wang, Y. S. Jung, K. J. Lee, *Nano Lett.* **2014**, 14, 7031.
- [14] D. Kim, S.-B. Jeon, J. Y. Kim, M.-L. Seol, S. O. Kim, Y.-K. Choi, *Nano Energy* **2015**, 12, 331.
- [15] X. He, H. Guo, X. Yue, J. Gao, Y. Xi, C. Hu, *Nanoscale* **2015**, 7, 1896.
- [16] X.-S. Zhang, M.-D. Han, R.-X. Wang, B. Meng, F.-Y. Zhu, X.-M. Sun, W. Hu, W. Wang, Z.-H. Li, H.-X. Zhang, *Nano Energy* **2014**, 4, 123.
- [17] K. Y. Lee, J. Chun, J.-H. Lee, K. N. Kim, N.-R. Kang, J.-Y. Kim, M. H. Kim, K.-S. Shin, M. K. Gupta, J. M. Baik, S.-W. Kim, *Adv. Mater.* **2014**, 26, 5037.
- [18] H. Y. Li, L. Su, S. Y. Kuang, C. F. Pan, G. Zhu, Z. L. Wang, *Adv. Funct. Mater.* **2015**, 25, 5691.
- [19] S. Wang, L. Lin, Z. L. Wang, *Nano Lett.* **2012**, 12, 6339.
- [20] S. Niu, S. Wang, L. Lin, Y. Liu, Y. S. Zhou, Y. Hu, Z. L. Wang, *Energy Environ. Sci.* **2013**, 6, 3576.
- [21] S. Niu, Y. Liu, X. Chen, S. Wang, Y. S. Zhou, L. Lin, Y. Xie, Z. L. Wang, *Nano Energy* **2015**, 12, 760.
- [22] S. Niu, Y. Liu, S. Wang, L. Lin, Y. S. Zhou, Y. Hu, Z. L. Wang, *Adv. Funct. Mater.* **2014**, 24, 3332.
- [23] S. Niu, Z. L. Wang, *Nano Energy* **2015**, 14, 161.
- [24] F. A. Rizk, G. N. Trinh, *High Voltage Engineering*, CRC Press, Boca Raton, FL **2014**.
- [25] M. S. Naidu, V. Kamaraju, *High Voltage Engineering*, Tata McGraw-Hill, New Delhi, India **2004**.
- [26] V. A. Dmitriev, K. G. Irvine, C. H. Carter, N. I. Kuznetsov, E. V. Kalinina, *Appl. Phys. Lett.* **1996**, 68, 229.
- [27] S. J. A. Koh, X. Zhao, Z. Suo, *Appl. Phys. Lett.* **2009**, 94, 262902.
- [28] S. Wang, S. Niu, J. Yang, L. Lin, Z. L. Wang, *ACS Nano* **2014**, 8, 12004.
- [29] Y. Yang, H. Zhang, Z.-H. Lin, Y. S. Zhou, Q. Jing, Y. Su, J. Yang, J. Chen, C. Hu, Z. L. Wang, *ACS Nano* **2013**, 7, 9213.

- [30] Y. S. Zhou, Y. Liu, G. Zhu, Z.-H. Lin, C. Pan, Q. Jing, Z. L. Wang, *Nano Lett.* **2013**, *13*, 2771.
- [31] C. Wu, T. W. Kim, H. Y. Choi, *Nano Energy* **2017**, *32*, 542.
- [32] M. A. Lieberman, A. J. Lichtenberg, *Principles of Plasma Discharges and Materials Processing*, John Wiley & Sons, Hoboken, NJ **2005**.
- [33] Y. Li, Y. H. Li, Q. X. Li, Y. Y. Zi, *J. Tsinghua Univ.* **2003**, *43*, 1024.
- [34] Z. Wen, M.-H. Yeh, H. Guo, J. Wang, Y. Zi, W. Xu, J. Deng, L. Zhu, X. Wang, C. Hu, L. Zhu, X. Sun, Z. L. Wang, *Sci. Adv.* **2016**, *2*, e1600097.
- [35] J. Chen, Y. Huang, N. Zhang, H. Zou, R. Liu, C. Tao, X. Fan, Z. L. Wang, *Nat. Energy* **2016**, *1*, 16138.
- [36] J. Bae, J. Lee, S. Kim, J. Ha, B.-S. Lee, Y. Park, C. Choong, J.-B. Kim, Z. L. Wang, H.-Y. Kim, J.-J. Park, U. I. Chung, *Nat. Commun.* **2014**, *5*, 4929.
- [37] L. Zhang, Y. Yu, G. P. Eyer, G. Suo, L. A. Kozik, M. Fairbanks, X. Wang, T. L. Andrew, *Adv. Mater. Technol.* **2016**, *1*, 1600147.
- [38] C. Wu, X. Wang, L. Lin, H. Guo, Z. L. Wang, *ACS Nano* **2016**, *10*, 4652.
- [39] Y. Zi, J. Wang, S. Wang, S. Li, Z. Wen, H. Guo, Z. L. Wang, *Nat. Commun.* **2016**, *7*, 10987.
- [40] S. Niu, X. Wang, F. Yi, Y. S. Zhou, Z. L. Wang, *Nat. Commun.* **2015**, *6*, 8975.
- [41] Y. Zi, H. Guo, J. Wang, Z. Wen, S. Li, C. Hu, Z. L. Wang, *Nano Energy* **2017**, *31*, 302.
- [42] E. Husain, R. S. Nema, *IEEE Trans. Electr. Insul.* **1982**, *EI-17*, 350.
- [43] J. Yang, J. Chen, Y. Liu, W. Yang, Y. Su, Z. L. Wang, *ACS Nano* **2014**, *8*, 2649.
- [44] L.-B. Huang, G. Bai, M.-C. Wong, Z. Yang, W. Xu, J. Hao, *Adv. Mater.* **2016**, *28*, 2744.
- [45] H. Guo, Z. Wen, Y. Zi, M.-H. Yeh, J. Wang, L. Zhu, C. Hu, Z. L. Wang, *Adv. Energy Mater.* **2016**, *6*, 1501593.